Article

Direct Growth of Binder-Free CNTs on a Nickel Foam Substrate for Highly Efficient Symmetric Supercapacitors

Melkiyur Isacfranklin, Yuvakkumar Rathinam,* Ravi Ganesan, and Dhayalan Velauthapillai*

Cite This: ACS Omega 2023, 8, 11700−11708

Read Online

ACCESS | ıll Metrics & More | 📄 Article Recommendations

ABSTRACT: In the modern civilized world, energy scarcity and associated environmental pollution are the center of focus in the search for reliable energy storage and harvesting devices. The need to develop cheaper and more competent binder-free electrodes for high-performance supercapacitors has attracted considerable research attention. In this study, two different procedures are followed to enhance the growth of carbon nanotubes (CNT-E and CNT-NF) directly coated on a Ni-foam substrate by a well-functioning chemical vapor deposition (CVD) method. Thus, directly grown optimized CNT electrodes are used as electrodes for electrochemical devices. Furthermore, solid-state symmetric supercapacitors are fabricated using CNT-NF//CNT-NF, and fruitful results are obtained with maximum specific capacitance (250.51 F/g), energy density (68.19 Wh/kg), and power density (2799.77 W/kg) at 1 A/g current density. The device exhibited good cyclic stability, with 92.42% capacitive retention and 99.68% Coulombic efficiency at 10 000 cycles, indicating the suitability of the electrodes for practical applications. This study emphasizes the importance of studying the direct growth of binder-free CNT electrodes to understand the actual behavior of electrodes and the proper storage mechanism.
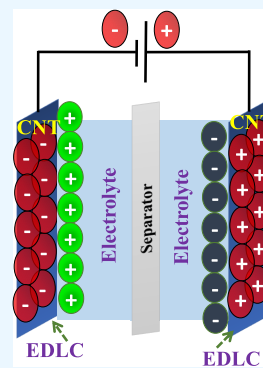
1. INTRODUCTION

The low availability and high utilization of renewable energy resources has led to accelerated research to find alternative sources.[1,2] Supercapacitors with a high charge/discharge rate and excellent cyclic life are not only excellent power sources but also reliable in energy storage devices.[3,4] With significant advances in various optoelectronic and portable electronic markets, research has intensified to identify potential electrodes for supercapacitors. The best electrode for use in supercapacitors should have the features of inexpensiveness, nontoxicity, high-capacitance performance, and long-lasting cycles.[5−7] Electrochemical double-layer capacitors (EDLCs) and pseudocapacitors are two major types of supercapacitors with diverse charge storage mechanisms. EDLCs follow a mechanism based on non-faradic processes, i.e., electrical absorption of electrolytic ions at the electrode/electrolyte interface. Reversible multielectron redox faradic reaction mechanisms occur in pseudocapacitors by which the specific capacitance and energy density can be determined.[8−10] Electrochemical double-layer capacitors (EDLCs) have many desirable features such as increased power density, security, fast charge/discharge capacity, digital communication ability, applicability in electric vehicles, memory backup, uninterruptible power sources, etc.[11,12] In general, carbon nanostructured materials in electrochemical double layer capacitors are the most preferred electrodes because of their extremely elevated surface area and high electron mobility. Among the several carbon materials, because of the elevated surface area, large pore size, low electronic and ionic charge-transfer resistance, high chemical stability, and electrical conductivity, carbon

nanotubes (CNTs) act as potential electrode materials in supercapacitors.[13−15] In particular, CNTs help recover the efficiency of the charge/discharge process by improving conductivity. Also, the use of a binder controls the electrical conductivity of the electrode, which is not required in this case.[16,17] Therefore, this synthesis technique uses the sophisticated chemical vapor deposition method to precipitate carbon molecules directly on a suitable substrate without the use of any other additives. In general, the process of chemical vapor deposition involves the reaction of a volatile precursor inserted into a horizontal furnace quartz tube (usually under vacuum). The furnace is heated up to the reaction temperature at which the precursor gas breaks down into a required material or desired coating and binds to the surface of the substrate material.[18,19] On injecting the precursor gas during the processing time, the coating material forms on the surface, and the exposed substrate forms coatings across the surface.[20] As a result of its eco-friendliness and high carbon yield on the substrate surface, the CVD process is preferred in a variety of commercial applications, and it is in fact the least expensive and scalable method for the mass production of CNTs.[21] In addition, methane, ethylene, acetylene, xylene, benzene, and
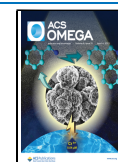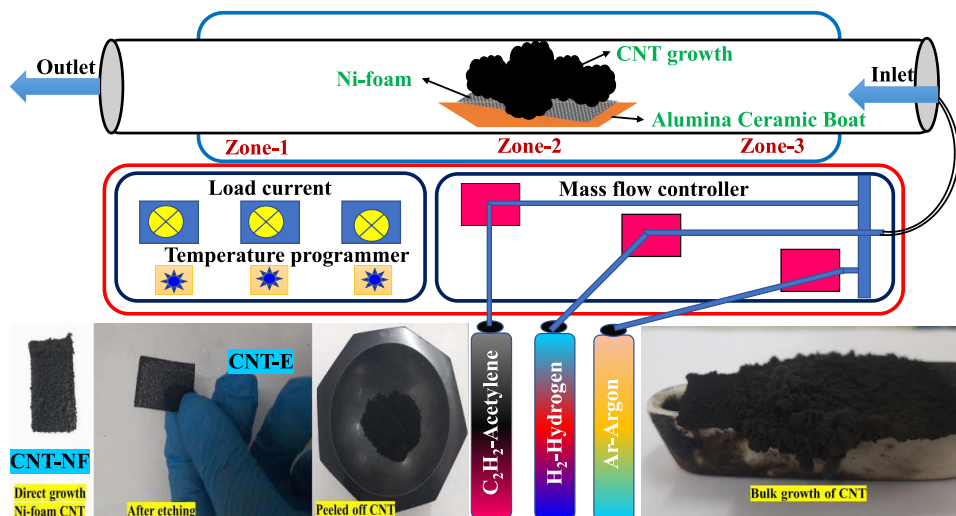
Scheme 1. Preparation of the Carbon Nanotube

carbon monoxide are commonly used CNT precursors. According to previous knowledge from the literature, acetylene is a well-known precursor gas to tailor the molecular structure and morphology of CNTs grown in low temperate (600−900 °C) ranges.[22,23] Three types of CNT purification procedures, including chemical, physical, and a combination of both, have been used to purify CNTs. The chemical purification process was useful due to its selectivity, cost-effectiveness, easy availability, and fast kinetics of oxidation of carbonaceous impurities from pristine CNTs, whereas the physical purification process is quite complex, time-consuming, and less effective in removing carbon impurities. KOH, H_2O_2, and HCl are all simple wet chemicals readily available in laboratories.[24] Here, we used HCl to etch the obtained CNT for the purification process. Nevertheless, due to the advantages of the CVD method, such as high yield, high deposition rate, nearly 100% purity and density, and high quality, high-performance CNTs are directly deposited on the well-suited Ni-foam substrate. Also, it is economical to manufacture and relatively easier to carry out chemical reactions on the surface of the substrate compared with physical modification. Compared with the etched CNT, directly grown bulk CNTs display improved electrochemical performances. Wei Wang et al. fabricated three-dimensional (3D) few-layered graphene/multiwalled carbon nanotubes (MWNTs). They fabricated symmetric supercapacitors with a high specific capacitance of 286 F/g. A capacity retention of 99.34% was maintained after 85 000 charge−discharge cycles.[25] Zheng et al. demonstrated low-temperature (550 °C) growth of the 3D network of graphene on Ni-foam in the CVD method. The fabricated device delivered a high gravimetric capacitance of 390 F/g at 0.03 A/g.[26] Chen et al. prepared N and Se codoped graphene aerogel (NSeGA) as a binder-free electrode, exhibiting a specific capacity of 302.9 F/g at 1 A/g and >94% capacity retention after 12,000 cycles. They constructed an NSeGA//NSeGA symmetric supercapacitor that exhibited 26.3 W h/kg energy density at 900 W/kg power density.[27] In the present study, we have effectively grown a one-dimensional carbon nanotube (CNT) directly on a Ni-foam substrate without the addition of a catalyst using a template-directed chemical vapor deposition method with outstanding graphitization, employing acetylene

as the carbon source. The specific capacitance, rate capability, capacitive retention, electrolyte, and charge-transfer resistance of the directly grown CNTs are studied by electrochemical analysis. It is clearly observed that the directly grown CNT on nickel foam (CNT-NF) exhibits morphologically excellent and elongated CNTs without any distortions compared with the HCl-etched CNT (CNT-E). The electrochemical performances of CNT-E and CNT-NF are studied, and the fabricated CNT-NF//CNT-NF solid-state device exhibits an elevated specific capacitance, high-quality cycling stability, and energy and power density. Hence, such a directly grown CNT electrode material is recommended as an inexpensive and promising candidate for supercapacitor applications.

2. EXPERIMENTAL PROCEDURE

2.1. Materials. Reagents used were of analytical purity. Ni-foam (1.6 mm × 200 mm × 300 mm; 110 ppi pore size is 0.23 mm) was purchased from Xiamen Zopin New Material Limited, China. Argon (Ar), hydrogen (H_2), and acetylene (C_2H_2) were obtained from Sastha gas company Ltd.
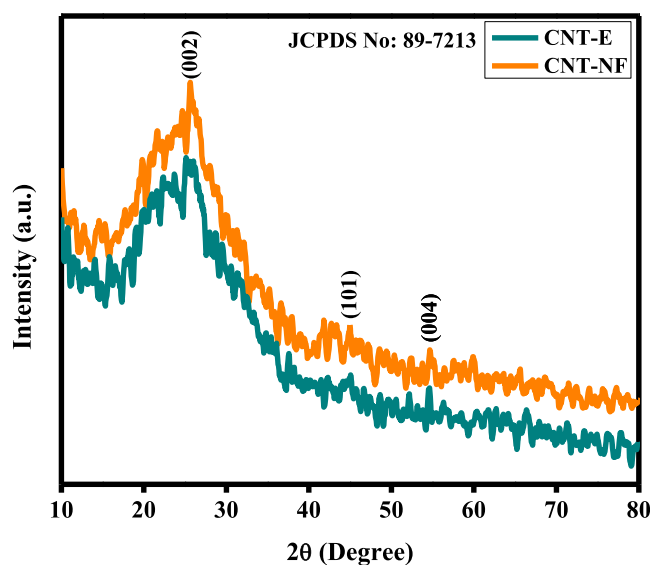

Figure 1. XRD patterns of CNT-E and CNT-NF.

Hydrochloric acid (HCl, 36−38%, analytical purity), ethanol, and methanol were acquired from Sisco Research Laboratories Pvt. Ltd.

2.2. Carbon Nanotube Synthesis by Chemical Reduction. A step-by-step approach was followed to grow carbon nanotubes on Ni-foam directly in the chemical vapor deposition unit. Before that, the CVD system was thermally annealed in an Ar atmosphere. The $(5 \times 5 \text{ cm}^2)$ $(1 \times 2 \text{ cm}^2)$ Ni-foam was ultrasonically cleaned well with HCl, ethanol, and methanol and dried in a vacuum air oven. The well-cleaned Ni-foam was placed horizontally in the center zone of the three-zone quartz tube CVD system on a quartz boat. Thereafter, the CVD system was closed and vacuumized using a vacuum pump unit. Then, the quartz tube was filled with Ar gas by proper control of gas flow (100 sccm) using a mass flow controller. After that, H_2 gas was purged into the CVD tube with a gas flow of 50 sccm. For the direct growth of CNTs, the whole reaction was executed under optimized conditions of 700 °C with a temperature increment of 5 °C per min. The acetylene (C_2H_2) carbon precursor was introduced at a gas flow rate of 40 sccm after reaching 700 °C. The reaction time was optimized to 20 min, and then, the whole setup was naturally cooled in an Ar atmosphere. After taking it out, the grown CNT was peeled off from the Ni-foam, etched with HCl, and rinsed several times with DI water, ethanol, and methanol, respectively; the product was named CNT-E; the second condition was obtaining the well-grown CNT on the Ni-foam substrate directly used as an electrode, which was named CNT-NF. The directly grown CNT on Ni-foam was employed as the current collector electrode (Scheme 1).

2.3. Characterization Tools. An X' Pert Pro—PAnalytic with Cu Kα radiation $(\lambda = 1.5418 \text{ Å})$ at 40 kV and 20 mA was used to analyze the structure of CNT materials. An Imaging Spectrograph STR 500 mm, Varian Cary Eclipse Photo Luminescence spectrometer, and a Thermo Nicolet 380 FTIR spectrometer were used to study the vibrational modes of CNT materials. Scanning electron microscopy (SEM, CAREL ZEISS, EVO 18) and high-resolution transmission electron microscopy (JEOL Japan, JEM-2100 plus) were employed to observe the surface morphology of the synthesized CNT. A BET Surface Area Analyzer quantachrome, Autosorb iQ2, was used to perform BET measurements. Electrochemical measurements of three-electrode devices included cyclic voltammetry (CV), galvanostatic charge−discharge (GCD), and electrochemical impedance spectroscopy (EIS). The performances of a solid-state symmetric supercapacitor using two electrodes was determined using a Biologic SP-150 instrument.

2.4. Electrochemical Measurements. The synthesized CNT-E and CNT-NF were systematically studied by various electrochemical techniques. Three-electrode performances were explored in a 2M KOH aqueous electrolyte including CNT-E and CNT-NF, saturated Ag/AgCl, and platinum wire as active, reference, and counter electrodes, respectively. For two-electrode performances, the electrolyte was composed of the synthetic polymer poly(vinyl alcohol) (PVA) (3 g) and 2 M KOH, and the concentration was fixed at 1:2 wt %. The cell consisted of a sandwich-like matrix, where the two symmetric electrodes were separated with a separator as a gel electrolyte was injected in between. The potential range for CV and GCD tests was set to −0.4−0.3 V in the three-electrode system and the optimized potential window was set to 0−1.4 V in the two-electrode system.[28]

3. RESULTS AND DISCUSSION

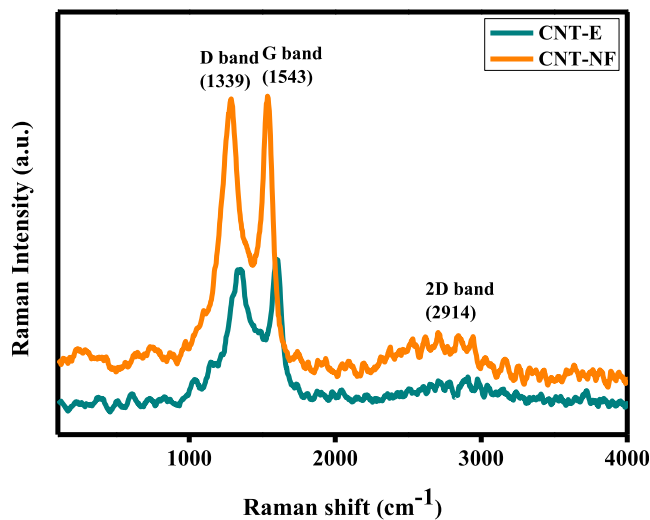Figure 1 displays the XRD patterns of as-prepared CNT-E and CNT-NF samples. XRD results indicate that the major peak

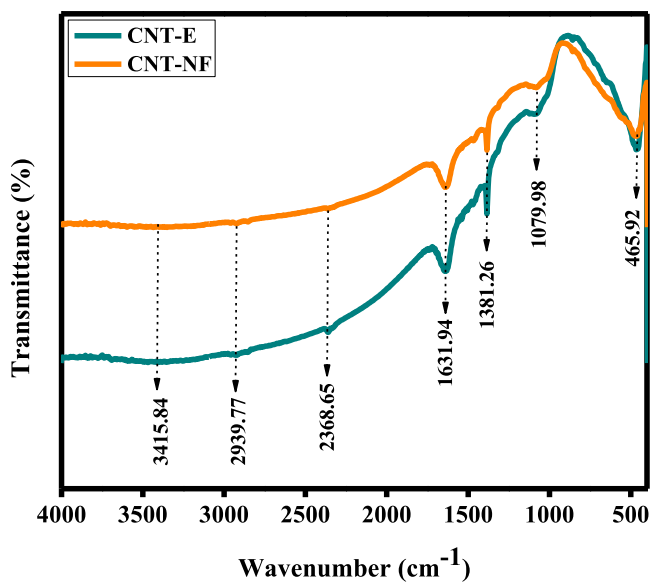**Figure 2.** Raman spectra of CNT-E and CNT-NF.

Figure 3. Fourier transform infrared spectra of CNT-E and CNT-NF.

observed at 26.15° is attributable to the (002)* *hkl* plane and the minor peaks at 44.89° (101) and 54.71° (004) signify that the carbon content (PDF # 89-7213) belongs to the hexagonal system of the space group *P*63/*mmc* (194). Compared with CNT-NF, CNT-E shows lower intensity, which reveals reduced growth of CNTs because of the presence of amorphous carbon (C).[29]

Raman analysis is one of the most important tools to identify the Raman spectrum of carbon nanotubes (CNTs) in a one-dimensional system. Figure 2 displays the Raman spectra of CNT-E and CNT-NF. Compared with the acid-treated CNT, the CNT directly formed on Ni-foam revealed high intensity and a slight blue shift of the peak. The noticeable D and G peaks around 1339 cm^{-1} (D band) and 1543 cm^{-1} (G band) are related to the concentration or measure of disorders of defects in C−C bonds in graphitic samples. In addition, these
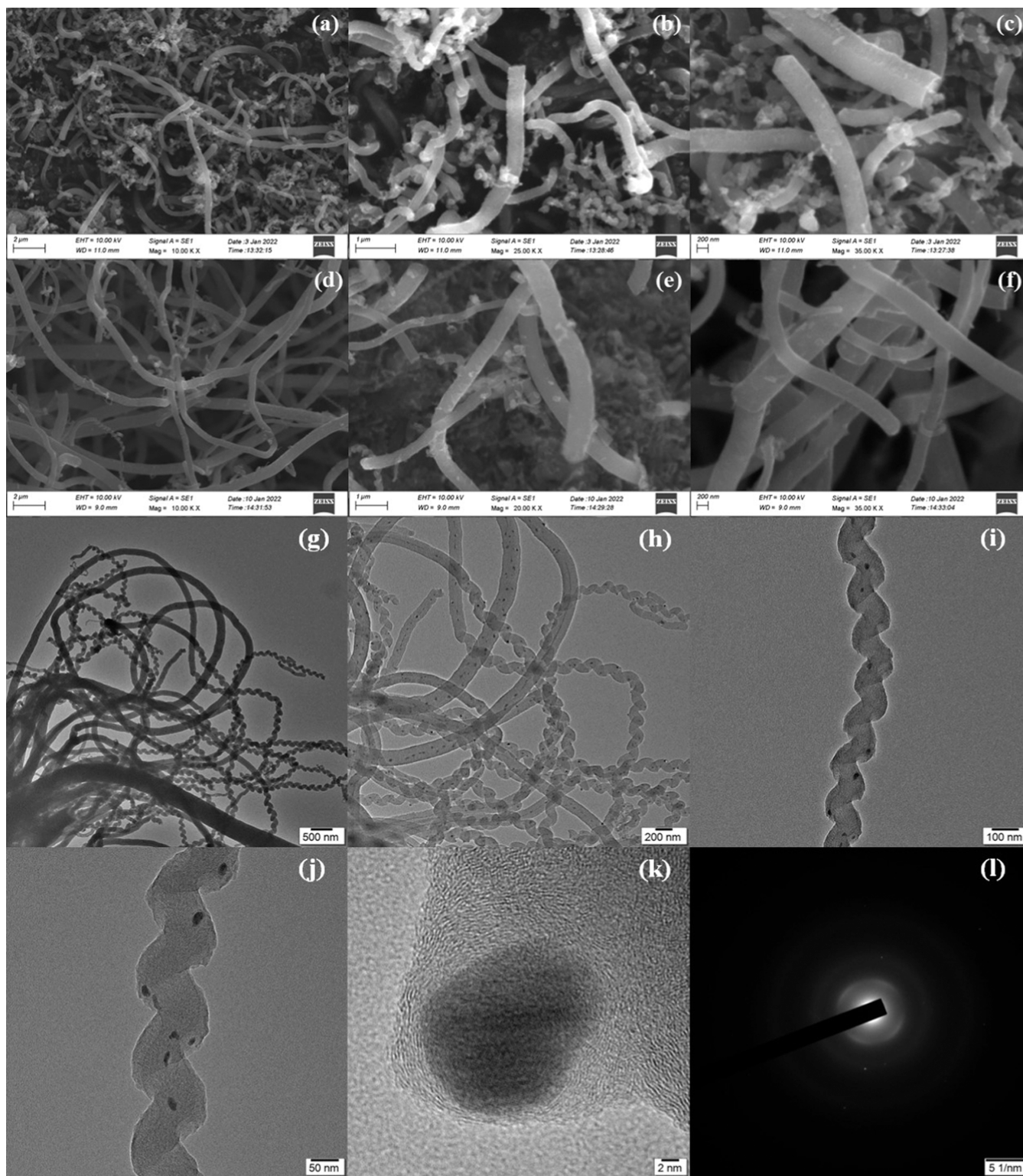
Figure 4. SEM images of (a–c) CNT-E and (d–f) CNT-NF; (g–l) HR-TEM images of CNT-NF.

peaks represent the degree of graphitization or metallicity of the graphitic content because of in-plane vibrations of C−C bonds. The I_D/I_G band peak intensity ratios of CNT-E and CNT-NF were estimated to be 0.8340 and 0.8403, respectively. A higher I_D/I_G ratio indicates an increase in the CNT defect concentration.[30]

Fourier transform infrared (FTIR) analysis was performed to detect the presence of carbon additives, contaminants, and functional elements in carbon nanotubes in the range of 400−4000 cm^{-1}. Figure 3 displays the FTIR spectra of CNT-E and CNT-NF. Both samples exhibited almost similar FTIR spectra except for the intensity. Peaks were observed at 465.92, 1079.98, 1381.28, 1631.94, 2368.65, 2939.77, and 3415.84 cm^{-1}. The peak at 1631.94 cm^{-1} arises because of the carbonyl functional group of C═O and C═C. The C−O, C−H, and O−H stretching vibration peaks are positioned at 1079.98,
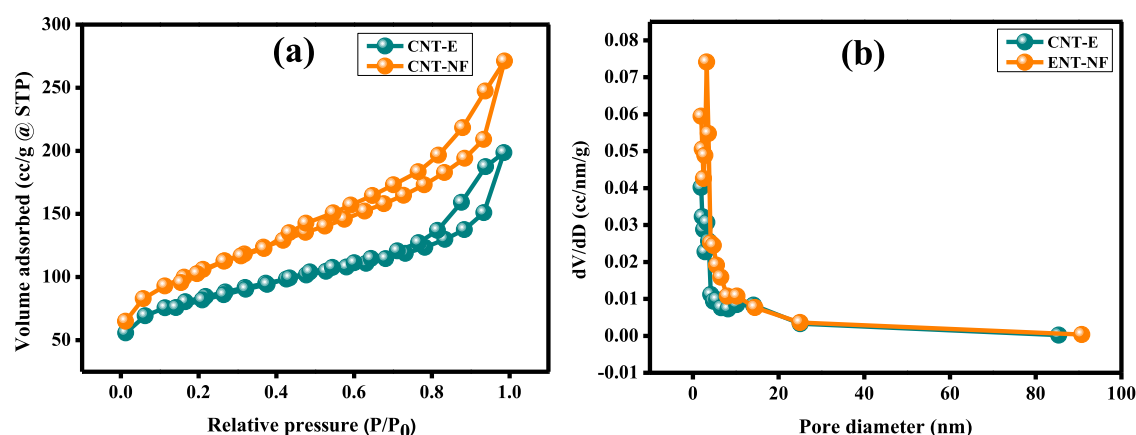
Figure 5. (a) N_2 adsorption−desorption isotherm and (b) BJH pore size distribution of CNT-E and CNT-NF.

2939.77, and 3415.84 cm^{-1}, respectively. The bending/stretching vibrations of the absorption bands of H−H groups are situated in the region of 1300−1700 cm^{-1}. Among the peaks mentioned above, the peak at 1381.28 cm^{-1} indicated -CH$_3$ stretching vibrations. In addition, the peak of 2939.77 cm^{-1} indicated stretching vibrations of chemisorbed hydrogen CH−CH$_3$ groups.[31,32]

Figure 4 presents SEM micrographs of CNTs prepared by two different processing methods, including acid-treated CNTs and directly grown CNTs on Ni-foam. CNT-E is entangled and clustered with a few cracks several microns in length (Figure 4a−c). On the other hand, directly grown CNT-NF revealed a low degree of entanglement and is clustered with a few cracks several microns in length, as illustrated in Figure 4d−f. This lower degree of entanglement in CNT-NF helps elongate the length of the nanotube and causes surface oxidation, which is highly favorable for rapid diffusion and ion migration at the electrode/electrolyte interface, thereby improving the electrochemical performance of supercapacitors using the CNT-NF electrode.[33,34] Figure 4g−l shows the HR-TEM images of well-formed thick and highly curled carbon nanotubes with different magnifications. The HR-TEM image in Figure 4g−j confirms that the CNTs are strongly helical, exhibit a small inner-wall diameter, and have a fishbone or bamboo structure. For growth carried out at 700 °C, twisted CNTs with an average diameter of 215 nm were mostly observed. The directly grown CNTs have relatively large inner (∼132 nm) and outer diameters (∼231 nm) from the Ni-foam substrate.

The Brunauer−Emmett−Teller (BET) analysis was used to estimate the specific surface area of materials from the nitrogen adsorption isotherms. Figure 5a shows type IV isotherms of the nitrogen adsorption and desorption isotherm of CNT-NF, confirming the mesoporous nature of the twisted, helical, and interlaced structure. Figure 5b displays pore size distribution by the Barrett−Joyner−Halenda (BJH) method, indicating a pore diameter of approximately 3−4 nm. The CNT-E electrode material possesses a surface area of 156.558 m^2/g, a pore volume of 0.245 cc/g, and a pore diameter of 1.940 nm. Comparatively, the CNT-NF electrode has higher surface area (258.251 m^2/g), pore volume (0.365 cc/g), and pore diameter (3.236 nm), with its open pore structure allowing easy access of dissolved ions to the electrode/electrolyte interface, which is important for the charging electrical double layer.[35]

3.1. Electrochemical Performances of the Three-Electrode Arrangement. The acid-treated CNT (CNT-E)

and directly grown CNT on Ni-foam substrate (CNT-NF) were subjected to cyclic voltammetry (CV) analysis in 2 M KOH in the potential range of −0.4 to 0.3 V at 10−100 mV/s. Figure 6a,b displays rectangular-shaped cyclic voltammograms of as-prepared electrodes, which clearly represent the capacitive behavior of the EDLC. This also undoubtedly specifies that the electrode has good electrical capacitance properties and good reversibility. Because of the high deposition rate, thick coatings on Ni-foam substrates are relatively easy to trigger chemical reactions on the substrate surface. Apparently, CNT-NF generated a larger output current than CNT-E, resulting in improved capacitance. The specific capacitance (C_s) was estimated from the three-electrode arrangement of CV curves at various scan rates employing the following formula: $C_s = \frac{\int I \times dV}{2 \times m \times v \times (V_f - V_i)}$ (F/g).[36] The estimated specific capacitances are 467.61 and 528.57 F/g at 10 mV/s for CNT-E and CNT-NF, respectively. All of the remaining scan rate values are shown in Table 1.

The capacitance behaviors of the as-prepared CNT-E and CNT-NF electrodes were electrochemically tested using GCD in the potential range of −0.4 to 0.3 V at 1−6 A/g. As illustrated in Figure 6c,d, charging and discharging curves of the two electrodes formed a perfect triangular shape and were almost symmetrical to their corresponding current density curves. The specific capacitance from the GCD curves in the three-electrode system was calculated using $C_s = \frac{I \times \Delta t}{m \times (V_f - V_i)}$, where I, Δt, m, and Δv have their usual meanings.[37] The calculated specific capacitance values were 354.50 and 436.81 F/g at 1 A/g. All remaining specific capacitance values of other current densities are listed in Table 2. The charge−discharge studies proved that CNT-NF is better than CNT-E. Further, the grown CNT-NF electrode was used for electrochemical stability analysis (Figure 6e). For 6000 continuous charge−discharge cycles, the CNT-NF electrodes delivered 99.41% capacitive retention, which shows the potential for utilization of the CNT electrodes in supercapacitor applications.

Electrochemical impedance spectroscopy (EIS) was employed to study the charge-transfer kinetics of the prepared CNT-E and CNT-NF electrodes from 100 kHz to 0.01 Hz at an amplitude of 10 mV. In both electrodes, the appearance of an incomplete semicircle and the oblique line respectively in the high- and low-frequency regions represent the interfacial charge-transfer resistance (Rct) and Warburg resistance (Wd) because of electrolyte ion diffusion, as shown in Figure 6f. The
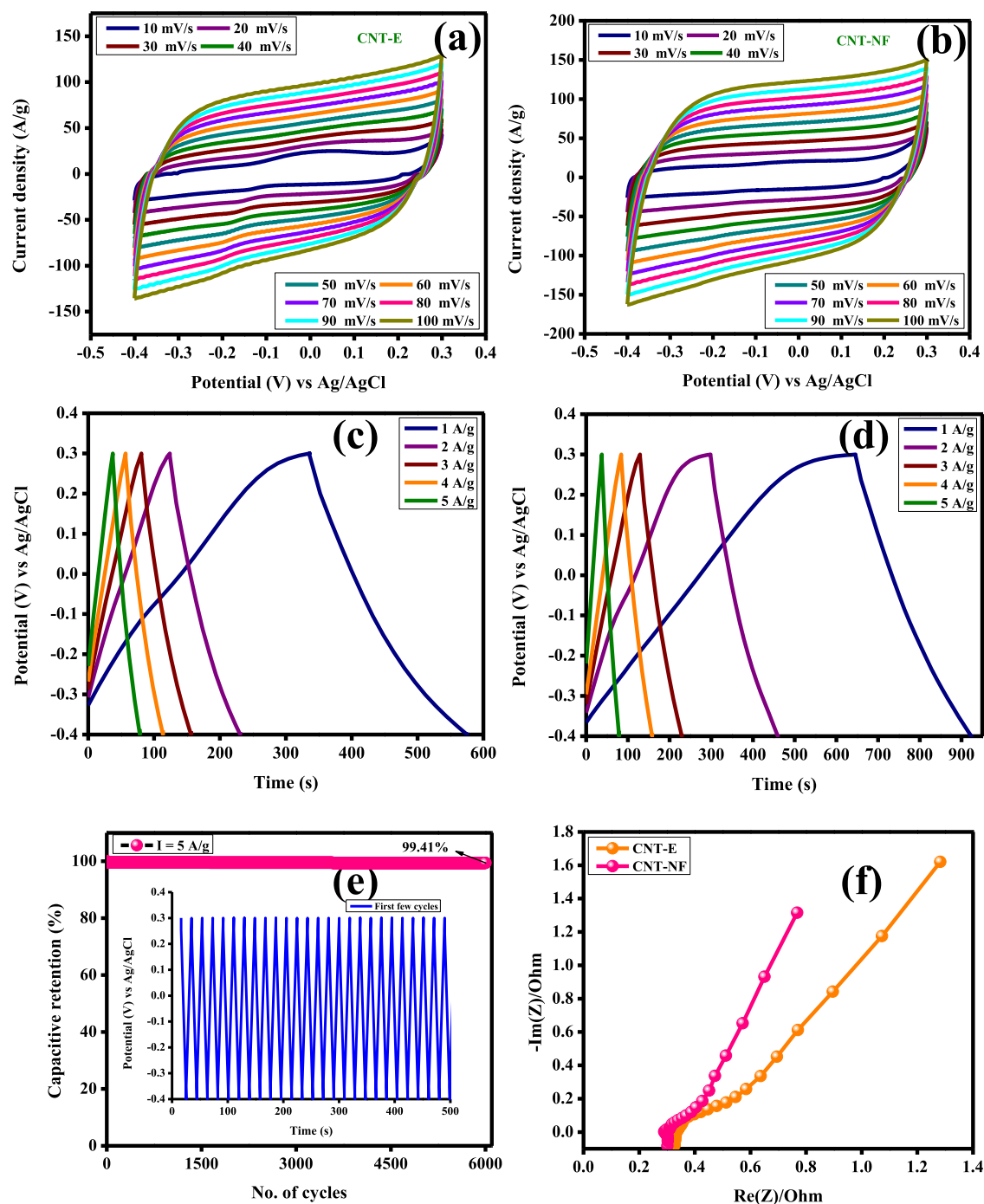
Figure 6. Cyclic voltammograms of (a) CNT-E and (b) CNT-NF; GCD analysis of (c) CNT-E and (d) CNT-NF; (e) stability analysis; and (f) Nyquist plot.

outstanding capacitive behavior observed in the CNT-NF electrode compared with the CNT-E electrode is due to its small solution resistance (Rs), indicating the high electrical conductivity of the directly grown CNTs.[38] These test results show that the CNT-NF electrode is perfect for elevated ion diffusion in aqueous electrolytes, in good agreement with the CV and GCD results, indicating the high capacitance of CNTs as electrodes for energy storage.

3.2. Solid-State Symmetric Supercapacitor Applications. Figure 7 shows electrochemical performances of solid-state symmetric supercapacitor device where two identical CNT-NF electrode materials act as both the cathode and the

anode. The physical diagram of an as-fabricated solid-state symmetric supercapacitor is illustrated in Figure 7a. Initially, different voltage ranges were used, and 1.0−1.4 V was chosen as the desired range (Figure 7b). Increasing the voltage from 1.0 to 1.4 V stabilizes the curve and leads to an expanded winding area of the CV curves, which implies an increased charge storage capacity and increased energy density. This will have a humb on the anodic and cathodic sides, indicating that an oxidation and reduction reaction is occurring; therefore, the potential was fixed at a constant value of 1.4 V. Figure 7c shows that the different scans of solid-state symmetric supercapacitor devices vary from 10 to 150 mV/s in CV

Table 1. Specific Capacitance from CV Profiles

scan rate (mV/s)	potential ($V_f - V_i$) (V)	mass (g)	CNT-E		CNT-NF	
			integral area of the CV curve	specific capacitance (F/g)	integral area of the CV curve	specific capacitance (F/g)
10	0.7	0.003	19.64	467.61	22.20	528.57
20			32.99	392.73	40.06	476.90
30			45.13	358.17	56.18	445.87
40			56.27	334.94	70.73	421.01
50			67.15	319.76	83.98	399.90
60			77.26	306.58	96.24	381.90
70			86.77	295.13	107.8	366.66
80			95.88	332.91	118.64	411.94
90			104.41	276.21	128.95	341.13
100			112.77	268.50	138.87	330.64

Table 2. Specific Capacitance from GCD Profiles

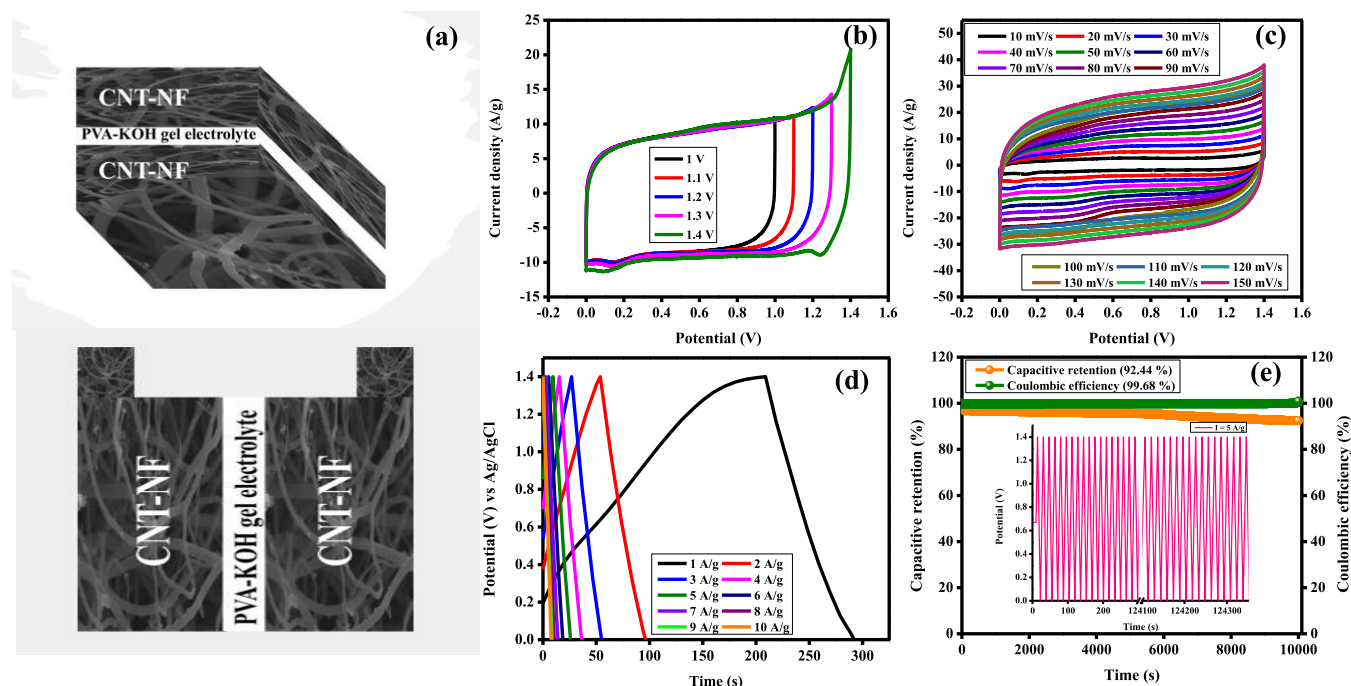| current density (A/g)	potential ($V_f - V_i$) (V)	mass (g)	CNT-E		CNT-NF	
			discharge time (Δt)	specific capacitance (F/g)	discharge time (Δt)	specific capacitance (F/g)
1	0.7	0.003	248.15	354.50	305.77	436.81
2			113.35	323.85	147.29	420.82
3			74.50	319.28	95.38	408.77
4			52.11	297.77	67.95	388.28
5			39.85	284.64	48.54	346.71

Figure 7. (a) Physical diagram of the assembled solid-state symmetric supercapacitor device; cyclic voltammetry analysis; (b) different potentials, (c) different scan rate variations, (d) GCD analysis, and (e) stability and efficiency of CNT-NF//CNT-NF.

curves, displaying a consistent performance even at high scan rates. Galvanic charge−discharge (GCD) tests were also performed at a constant potential of 1.4 V by varying the current density from 1 to 10 A/g, as displayed in Figure 7d. The increased voltage of 1.4 V gives electrode materials a longer discharge time, shows the great potential of the electrode materials to store energy, and ensures good Coulombic efficiency. The linearity of both CV and GCD (triangular shape) curves specifies the existence of a non-faradic process in the device ensuring the electric double-layer behavior of the device.[39] The following formulas are employed to estimate the specific capacitance, energy, and power density of the solid-state symmetric supercapacitor device

$$C_s = \frac{4 \times I \times \Delta t}{m \times \Delta V} \text{(F/g)}$$

$$E_d = \frac{CV^2}{2 \times 3.6} \text{(Wh/kg)}$$

Table 3. Solid-State Symmetric Supercapacitor Device Performances

current density (A/g)	discharge time (Δt)	specific capacitance (F/g)	energy density (Wh/kg)	power density (W/kg)
1	87.68	250.51	68.19	2799.77
2	42.43	242.45	66.00	5599.81
3	27.93	239.40	65.17	8400.00
4	20.80	237.71	64.70	11198.07
5	16.42	234.57	63.85	13998.78
6	13.18	225.94	61.50	16798.17
7	11.09	221.80	60.37	19597.11
8	9.48	202.24	55.05	20905.06
9	7.58	194.91	50.39	23931.92
10	6.03	172.28	46.89	27994.02

$$P_d = \frac{3600 \times E_d}{\Delta t} (W/kg)$$

where C_s is the total specific capacitance, Δt is the discharge time (s), m is the active material mass, V is the optimized potential window, and E_d and P_d are respectively the energy density and power density.[40,41] All estimated energy and power density values are summarized in Table 3. Figure 7e reveals the stability (capacitive retention of 92.44%) and columbic efficiency (99.68%) of the fabricated device over 10,000 consecutive charge−discharge cycles.

4. CONCLUSIONS

In summary, the chemical vapor deposition method was used to achieve binder-free direct growth of CNTs on a unique Ni-foam substrate using acetylene as the precursor gas. The binder-free CNT-NF electrode reveals an elevated specific capacitance (436.81 F/g@1 A/g) and good cyclic stability (99.41%@6000 charge−discharge cycles) in an aqueous electrolyte (2M KOH) medium. The as-assembled solid-state symmetric device delivered a high specific capacitance (250.51 F/g @ 1 A/g), energy density (68.19 Wh/kg @ 1 A/g), power density (27,994.02 W/kg @ 10 A/g), capacitive retention (92.42% @ 10,000 cycles), and Coulombic efficiency (99.68% @ 10,000 cycles) in a PVA and KOH gel electrolyte medium. This study presents an easy method to prepare binder-free functional materials with a well-controlled morphology of carbon materials (CNTs) and opens new pathways for their applications in high-performance practical supercapacitors and other emerging devices.

AUTHOR INFORMATION

Corresponding Authors

Yuvakkumar Rathinam − *Department of Physics, Alagappa University, Karaikudi 630003 Tamil Nadu, India;* orcid.org/0000-0001-6779-3453; Email: yuvakkumarr@alagappauniversity.ac.in

Dhayalan Velauthapillai − *Faculty of Engineering and Science, Western Norway University of Applied Sciences, Bergen 5063, Norway;* orcid.org/0000-0002-4162-7446; Email: dhayalan.Velauthapillai@hvl.no

Authors

Melkiyur Isacfranklin − *Department of Physics, Alagappa University, Karaikudi 630003 Tamil Nadu, India*

Ravi Ganesan − *Department of Physics, Alagappa University, Karaikudi 630003 Tamil Nadu, India; Adjunct Professor,*

Department of Physics, Chandigarh University, Mohali 140413 Punjab, India

Complete contact information is available at:
https://pubs.acs.org/10.1021/acsomega.2c04998

Notes

The authors declare no competing financial interest.

REFERENCES

(1) Olabi, A. G.; Abbas, Q.; Al Makky, A.; Abdelkareem, M.A. Supercapacitors as next generation energy storage devices: Properties and applications. *Energy* **2022**, *248*, No. 123617.

(2) Zhu, T.; Ding, J.; Shao, Q.; Qian, Y.; Huang, X. P,Se-Codoped MoS₂ Nanosheets as Accelerated Electrocatalysts for Hydrogen Evolution. *ChemCatChem* **2019**, *11*, 689−692.

(3) AlAreeqi, S.; Bahamon, D.; Polychronopoulou, K.; Vega, L.F. Insights into the thermal stability and conversion of carbon-based materials by using ReaxFF reactive force field: Recent advances and future directions. *Carbon* **2022**, *196*, 840.

(4) Zhan, J.; Li, G.; Gu, Q.; Wu, H.; Su, L.; Wang, L. Porous Carbon Nanosheets Armoring 3D Current Collectors toward Ultrahigh Mass Loading for High-Energy-Density All-Solid-State Supercapacitors. *ACS Appl. Mater. Interfaces* **2021**, *13*, 52519−52529.

(5) Blyweert, P.; Nicolas, V.; Fierro, V.; Celzard, A. 3D printing of carbon-based materials: A review. *Carbon* **2021**, *183*, 449−485.

(6) Isacfranklin, M.; Yuvakkumar, R.; Ravi, G.; Hong, S. I.; Velauthapillai, D.; Thambidurai, M.; Dang, C.; Algarni, T. S.; Al-Mohaimeed, A.M. Heterostructured SmCoO₃/rGO composite for high-energy hybrid supercapacitors. *Carbon* **2021**, *172*, 613−623.

(7) Kumar, R.; Joanni, E.; Sahoo, S.; Shim, J. J.; Kian, T. W.; Matsuda, A.; Singh, R. K. An overview of recent progress in nanostructured carbon-based supercapacitor electrodes: from zero to bi-dimensional materials. *Carbon* **2022**, *193*, 298.

(8) Jiao, S.; Liu, M.; Li, Y.; Abrha, H.; Wang, J.; Dai, Y.; Li, J.; Kang, N.; Li, Y.; Liu, X. Emerging hydrovoltaic technology based on carbon black and porous carbon materials: A mini review. *Carbon* **2022**, *193*, 339.

(9) Tian, W.; Li, Y.; Zhou, J.; Wang, T.; Zhang, R.; Cao, J.; Luo, M.; Li, N.; Zhang, N.; Gong, H.; Zhang, J.; et al. Implantable and biodegradable micro-supercapacitor based on a superassembled three-dimensional network Zn@ PPy hybrid electrode. *ACS Appl. Mater. Interfaces* **2021**, *13*, 8285−8293.

(10) Zhao, J.; Li, C.; Zhang, Q.; Zhang, J.; Wang, X.; Sun, J.; Wang, J.; Xie, J.; Lu, C.; Lu, W.; Yao, Y. All-solid-state hybrid supercapacitors based on ZnCo₂O₄ nanowire arrays and carbon nanorod electrode materials. *Carbon* **2017**, *123*, 676−682.

(11) Li, W.; Yang, X.; Chen, Z.; Lv, T.; Wang, X.; Qiu, J. Synthesis and structure regulation of armor-wearing biomass-based porous carbon: Suppression the leakage current and self-discharge of supercapacitors. *Carbon* **2022**, *196*, 136−145.

(12) Umezawa, S.; Douura, T.; Yoshikawa, K.; Takashima, Y.; Yoneda, M.; Gotoh, K.; Stolojan, V.; Silva, S.R.P.; Hayashi, Y.; Tanaka, D. Supercapacitor electrode with high charge density based on boron-doped porous carbon derived from covalent organic frameworks. *Carbon* **2021**, *184*, 418−425.

(13) Ouyang, J.; Wang, X.; Wang, L.; Xiong, W.; Li, M.; Hua, Z.; Zhao, L.; Zhou, C.; Liu, X.; Chen, H.; Luo, Y. Construction of a porous carbon skeleton in wood tracheids to enhance charge storage for high-performance supercapacitors. *Carbon* **2022**, *196*, 532−539.

(14) Zhu, M.; Shao, Q.; Pi, Y.; Guo, J.; Huang, B.; Qian, Y.; Huang, X. Ultrathin Vein-Like Iridium−Tin Nanowires with Abundant

Oxidized Tin as High-Performance Ethanol Oxidation Electrocatalysts. *Small* **2017**, *13*, No. 1701295.

(15) Hu, C.; Miao, L.; Yang, Q.; Yu, X.; Song, L.; Zheng, Y.; Wang, C.; Li, L.; Zhu, L.; Cao, X.; Niu, H. Self-assembly of CNTs on Ni foam for enhanced performance of NiCoO₂@CNT@ NF supercapacitor electrode. *Chem. Eng. J.* **2021**, *410*, No. 128317.

(16) Jian, X.; Li, H.; Li, H.; Li, Y.; Shang, Y. Flexible and freestanding MoS2/rGO/CNT hybrid fibers for high-capacity all-solid supercapacitors. *Carbon* **2021**, *172*, 132−137.

(17) Joshi, B.; Samuel, E.; Kim, Y. I.; Yarin, A. L.; Swihart, M. T.; Yoon, S.S. Review of recent progress in electrospinning-derived freestanding and binder-free electrodes for supercapacitors. *Coord. Chem. Rev.* **2022**, *460*, No. 214466.

(18) Kinoshita, T.; Karita, M.; Nakano, T.; Inoue, Y. Two step floating catalyst chemical vapor deposition including in situ fabrication of catalyst nanoparticles and carbon nanotube forest growth with low impurity level. *Carbon* **2019**, *144*, 152−160.

(19) Ding, E. X.; Liu, P.; Khan, A. T.; Zhang, Q.; Wei, N.; Jiang, H.; Kauppinen, E.I. Towards the synthesis of semiconducting single-walled carbon nanotubes by floating-catalyst chemical vapor deposition: Challenges of reproducibility. *Carbon* **2022**, *195*, 92−100.

(20) Hashempour, M.; Vicenzo, A.; Zhao, F.; Bestetti, M. Direct growth of MWCNTs on 316 stainless steel by chemical vapor deposition: Effect of surface nano-features on CNT growth and structure. *Carbon* **2013**, *63*, 330−347.

(21) Dong, X.; Li, B.; Wei, A.; Cao, X.; Chan-Park, M. B.; Zhang, H.; Li, L. J.; Huang, W.; Chen, P. One-step growth of graphene−carbon nanotube hybrid materials by chemical vapor deposition. *Carbon* **2011**, *49*, 2944−2949.

(22) Xing, B.; Zhao, J.; Ren, Y.; Pan, Q.; Song, J.; Han, P.; Ma, G. Hybrid Composite Materials Generated Via Growth of Carbon Nanotubes in Expanded Graphite Pores Using a Microwave Technique. *Inorg. Chem. Commun.* **2022**, *137*, No. 109185.

(23) Sivamaran, V.; Balasubramanian, V.; Gopalakrishnan, M.; Viswabaskaran, V.; Gourav Rao, A.; Selvamani, S.T. Carbon nanotubes, nanorings, and nanospheres: Synthesis and fabrication via chemical vapor deposition—a review. *Nanomater. Nanotechnol.* **2022**, *12*, No. 18479804221079495.

(24) Das, R.; et al. Common wet chemical agents for purifying multiwalled carbon nanotubes. *J. Nanomater.* **2014**, *2014*, 1−9.

(25) Wang, W.; Guo, S.; Penchev, M.; Ruiz, I.; Bozhilov, K. N.; Yan, D.; Ozkan, M.; Ozkan, C.S. Three dimensional few layer graphene and carbon nanotube foam architectures for high fidelity supercapacitors. *Nano Energy* **2013**, *2*, 294−303.

(26) Zheng, L.; Cheng, X.; Ye, P.; Shen, L.; Wang, Q.; Zhang, D.; Gu, Z.; Zhou, W.; Wu, D.; Yu, Y. Low temperature growth of three-dimensional network of graphene for high-performance supercapacitor electrodes. *Mater. Lett.* **2018**, *218*, 90−94.

(27) Chen, J.; Lin, C.; Zhang, M.; Jin, T.; Qian, Y. Constructing Nitrogen, Selenium Co-Doped Graphene Aerogel Electrode Materials for Synergistically Enhanced Capacitive Performance. *ChemElectroChem* **2020**, *7*, 3311−3318.

(28) Isacfranklin, M.; Yuvakkumar, R.; Kumar, P. S.; Thirumal, V.; Ravi, G.; Velauthapillai, D. Hydrogen free direct growth carbon nanorod as a promising electrode in symmetric supercapacitor applications. *Prog. Org. Coat.* **2022**, *158*, No. 106379.

(29) Vasudevan, D.; Senthilkumar, D.; Surendhiran, S. Performance and characterization studies of reduced graphene oxides aqua nanofluids for a pool boiling surface. *Int. J. Thermophys.* **2020**, *41*, 74.

(30) Melvin, G. J. H.; Ni, Q. Q.; Suzuki, Y.; Natsuki, T. Microwave-absorbing properties of silver nanoparticle/carbon nanotube hybrid nanocomposites. *J. Mater. Sci.* **2014**, *49*, 5199−5207.

(31) Jun, L. Y.; Mubarak, N. M.; Yon, L. S.; Bing, C. H.; Khalid, M.; Abdullah, E. C. Comparative study of acid functionalization of carbon nanotube via ultrasonic and reflux mechanism. *J. Environ. Chem. Eng.* **2018**, *6*, 5889−5896.

(32) Ţucureanu, V.; Matei, A.; Avram, A. M. FTIR spectroscopy for carbon family study. *Crit. Rev. Anal. Chem.* **2016**, *46*, 502−520.

(33) Ma, Z.; Wang, Y.; Yang, Y.; Yousaf, M.; Zou, M.; Cao, A.; Han, R. P. Flexible hybrid carbon nanotube sponges embedded with SnS₂ from tubular nanosheaths to nanosheets as free-standing anodes for lithium-ion batteries. *RSC Adv.* **2016**, *6*, 30098−30105.

(34) Wei, J.; Miao, Z.; Wang, Y.; Zhou, Y.; Gao, D.; Zhang, H.; Qiao, M. Boosting power factor of thermoelectric cementitious composites by a unique CNT pretreatment process with low carbon content. *Energy Build.* **2022**, *254*, No. 111617.

(35) Frackowiak, E.; Metenier, K.; Bertagna, V.; Beguin, F. Supercapacitor electrodes from multiwalled carbon nanotubes. *Appl. Phys. Lett.* **2000**, *77*, 2421−2423.

(36) Ali, G. A. M.; Habeeb, O. A.; Algarni, H.; Chong, K.F. CaO impregnated highly porous honeycomb activated carbon from agriculture waste: symmetrical supercapacitor study. *J. Mater. Sci.* **2019**, *54*, 683−692.

(37) Dadashi, R.; Bahram, M.; Faraji, M. Fabrication of a solid-state symmetrical supercapacitor based on polyaniline grafted multiwalled carbon nanotube deposit onto Created Vertically Oriented Graphene Nanosheets on graphite sheet. *J. Energy Storage* **2022**, *52*, No. 104775.

(38) Abbas, A.; Yi, Y. M.; Saleem, F.; Jin, Z.; Veksha, A.; Yan, Q.; Lisak, G.; Lim, T.M. Multiwall carbon nanotubes derived from plastic packaging waste as a high-performance electrode material for supercapacitors. *Int. J. Energy Res.* **2021**, *45*, 19611−19622.

(39) Tiwari, P.; Jaiswal, J.; Chandra, R. Hierarchal growth of MoS₂@ CNT heterostructure for all solid state symmetric supercapacitor: Insights into the surface science and storage mechanism. *Electrochim. Acta* **2019**, *324*, No. 134767.

(40) Zhou, Y.; Jin, P.; Zhou, Y.; Zhu, Y. High-performance symmetric supercapacitors based on carbon nanotube/graphite nanofiber nanocomposites. *Sci. Rep.* **2018**, *8*, 9005.

(41) Yu, J.; Yu, C.; Guo, W.; Wang, Z.; Ding, Y.; Xie, Y.; Liu, K.; Wang, H.; Tan, X.; Huang, H.; Qiu, J. Insight into the Effects of Current Collectors and In Situ Ni Leaching in High-Voltage Aqueous Supercapacitors. *Adv. Funct. Mater.* **2022**, *32*, No. 2204609.